ARL-TR-9236 ● JULY 2021

DEVCOM ARMY RESEARCH LABORATORY

A High-Fidelity, Roll-Dependent Aerodynamic Model for a Long-Range, High-Speed Missile

by Bradley T Burchett, Justin L Paul, Joseph D Vasile, and Joshua T Bryson

NOTICES

Disclaimers

The findings in this report are not to be construed as an official Department of the Army position unless so designated by other authorized documents.

Citation of manufacturer's or trade names does not constitute an official endorsement or approval of the use thereof.

Destroy this report when it is no longer needed. Do not return it to the originator.

ARL-TR-9236 ● JULY 2021

A High-Fidelity, Roll-Dependent Aerodynamic Model for a Long-Range, High-Speed Missile

Bradley T Burchett, Justin L Paul, Joseph D Vasile, and Joshua T Bryson
Weapons and Materials Research Directorate,
DEVCOM Army Research Laboratory

REPORT DOCUMENTATION PAGE

Form Approved
OMB No. 0704-0188

1. REPORT DATE *(DD-MM-YYYY)*	2. REPORT TYPE	3. DATES COVERED (From - To)
July 2021	Technical Report	10 November–14 May 2021

4. TITLE AND SUBTITLE
A High-Fidelity, Roll-Dependent Aerodynamic Model for a Long-Range, High-Speed Missile

5a. CONTRACT NUMBER

5b. GRANT NUMBER

5c. PROGRAM ELEMENT NUMBER

6. AUTHOR(S)
Bradley T Burchett, Justin L Paul, Joseph D Vasile, and Joshua T Bryson

5d. PROJECT NUMBER

5e. TASK NUMBER

5f. WORK UNIT NUMBER

7. PERFORMING ORGANIZATION NAME(S) AND ADDRESS(ES)
DEVCOM Army Research Laboratory
ATTN: FCDD-RLW-WD
Aberdeen Proving Ground, MD 21005

8. PERFORMING ORGANIZATION REPORT NUMBER
ARL-TR-9236

9. SPONSORING/MONITORING AGENCY NAME(S) AND ADDRESS(ES)

10. SPONSOR/MONITOR'S ACRONYM(S)

11. SPONSOR/MONITOR'S REPORT NUMBER(S)

12. DISTRIBUTION/AVAILABILITY STATEMENT
Approved for public release: distribution unlimited.

13. SUPPLEMENTARY NOTES
ORCID ID(s): Burchett, 0000-0002-1934-0537; Bryson, 0000-0002-0753-6823; Paul, 0000-0003-4133-7585; Vasile, 0000-0003-3812-6277

14. ABSTRACT
Several methods are applied to capture the roll-dependent aerodynamics of a high-speed missile. An inviscid computational fluid dynamics (CFD) solver is used over a large targeted test matrix to capture the effects of Mach number, angle of attack, actuator deflections, and aerodynamic roll on the aerodynamic forces and moments. In order to deploy the model to a simulation environment, the CFD results are smoothed using Fourier series, then fit to polynomial expansions in extensive tables. In order to support prediction of four independently controlled actuators, the effects due to deflection are modeled in a local actuator frame, then assembled in the body frame using superposition. The assembled model is validated through comparisons with an additional inviscid CFD prediction and wind tunnel data.

15. SUBJECT TERMS
onboard sensors, projectile aerodynamics, trajectory reconstruction, initial conditions, dual spin

16. SECURITY CLASSIFICATION OF:			17. LIMITATION OF ABSTRACT	18. NUMBER OF PAGES	19a. NAME OF RESPONSIBLE PERSON
a. REPORT	b. ABSTRACT	c. THIS PAGE			Bradley T Burchett
Unclassified	Unclassified	Unclassified	UU	45	19b. TELEPHONE NUMBER (Include area code) (812) 201-0390

Contents

List of Figures

List of Tables

1. Introduction

For several decades, researchers have predicted the roll-dependent aerodynamics of slightly asymmetric missiles to be modeled by a single harmonic equal in period to the roll angle between adjacent fins.[1–4] However, for the configuration studied in this report, forces and moments vary with roll in a more complicated fashion. Inviscid computational fluid dynamics (CFD) predicts oscillations in the pitch and yaw moments, for instance, which have a fundamental period that is a fraction of the roll angle between lifting surfaces. In order to capture these oscillations to an acceptable level of fidelity, a two-step process was contrived to find roll-dependent polynomial models of the forces and moments.

The high-speed, long-range Laboratory Technology Vehicle (LTV-1) depicted in Fig. 1 is designed for flight over a wide envelope from high subsonic to hypersonic speeds.[5] Four long strakes enhance the lift generated when flying at nonzero angles of attack. Trailing edge flaps are mounted at the tail in line with each strake. Each flap moves independently, allowing for maneuvers that include pitch, yaw, roll, and aerobraking.[6–8]

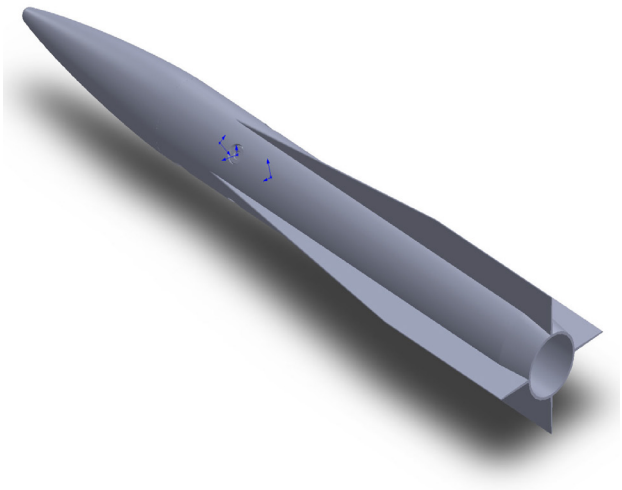

Fig. 1 The high-speed, long-range LTV-1

To accurately model the aerodynamics of LTV-1, an inviscid CFD solver is used to predict the forces and moments over a large matrix of flight conditions. Force and moment predictions are broken into separate components for the body (without flaps), components for a single flap alone, and a set of predictions for the entire build. Breaking the forces and moments into these separate contributions allows for the prediction of total forces and moments using an assembly process that will be discussed later. The single flap model can be applied to each of the flaps by

adjusting the input conditions and transforming the force/moment contribution to match the physical location of other flaps around the body.

The predictions from CFD were smoothed and interpolated using a novel approach based upon Fourier series. This postprocessing removed obvious outliers where the solver had not converged, enforced symmetry matching the vehicle's geometric symmetry, and ensured null points in the transverse forces and moments at appropriate points in the roll cycle. Due to the choice of harmonic basis functions for this interpolation, symmetry and null points were ensured by choosing the fundamental period of the harmonics to match the vehicle's roll symmetry. After smoothing and interpolation, each total force/moment component at a given Mach number is predicted as a function of angle of attack (AoA). These predictions are then used in a polynomial regression to obtain a polynomial model for each force/moment component at each given set of inputs. The result is a set of large look-up tables for the polynomial coefficients as functions of Mach, aerodynamic bank, and flap deflection.

This report also presents several validation methods used to check the model. First, the total forces and moments are assembled in a common frame using superposition. These totals are then compared to the CFD data set for the entire vehicle at several Mach numbers, angles of attack, and zero deflection. This step not only validates the assembly process, but also checks that interpolation and polynomial regression have not skewed the estimates in any significant way. Second, a set of wind tunnel tests on a subscale model were performed at Florida State University.[9] The results are compared to the assembled model for several configurations. Finally, tuning of the Fourier model to the wind tunnel data is explored using an approach from linear feedforward neural networks.

2. Approach: Inviscid CFD over a Large Test Matrix

This study began by first collecting data from simulations ran using a software package called Cart3D developed by NASA. NASA's Cart3D is an inviscid CFD package for aerodynamic design and analysis. Cart3D provides utility for surface modeling and intersection, mesh generation, flow simulation, and postprocessing.[10] The mesh generation software with the Cart3D package produces Cartesian meshes for arbitrarily complex, watertight geometries. The mesh generation process automatically increases the fidelity of the domain near small features and inflections present in the geometry to better resolve flow features near the surface. The option also exists to create higher-resolution areas in the wake of the body. Adjoint-based mesh adaption is also available to refine the mesh based on the flow

solution. Aerodynamic coefficients for a given flight condition (i.e., Mach number and aerodynamic angles) are computed in several minutes.

The meshes generated for the simulations numbered approximately 6.1 million cells. This was the result of using 14 levels of refinement in a cubical computational domain with an inscribed sphere of 14 body lengths. The meshes were also further refined using prescribed density boxes near the nose and near the body of the geometry. An example of one of the meshes is shown in Fig. 2.

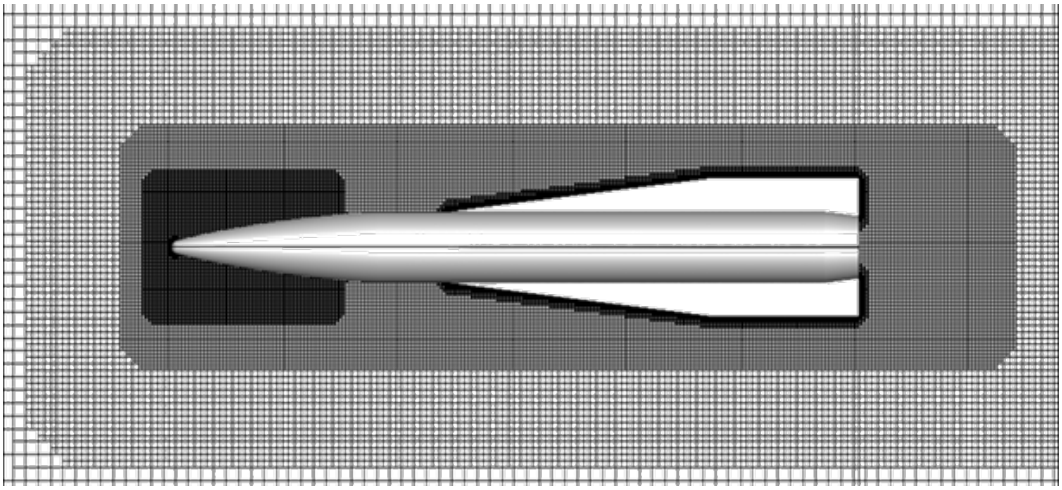

Fig. 2 Example Cart3D mesh

For all simulations, the geometry was oriented in the plus (+) configuration in the mesh with the deflectable flap set on the starboard side. This orientation characterizes the zero roll orientation ($\phi = 0°$). Positive deflection of the flap corresponds to counterclockwise rotation as viewed from the starboard side while negative flap deflection is the opposite rotation. This is best illustrated in Fig. 3.

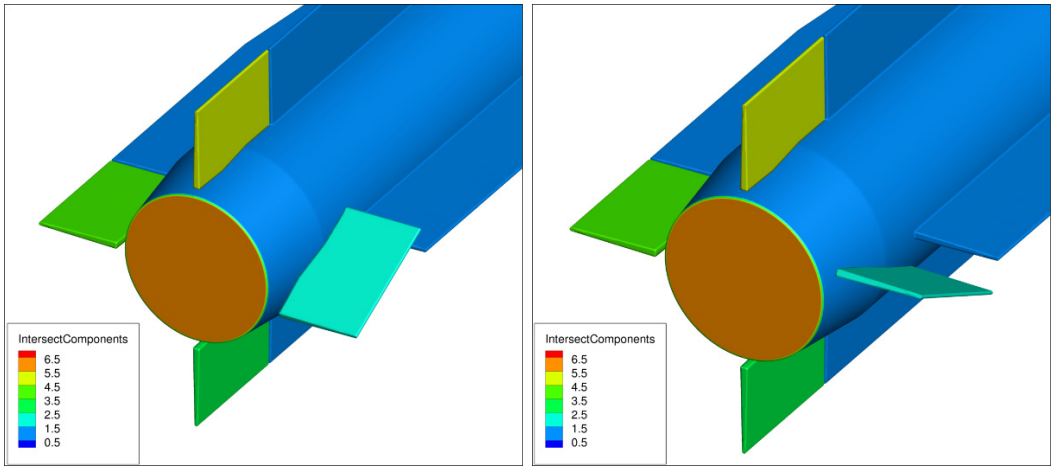

Fig. 3 Positive flap deflection, δ = 25° (left) and negative flap deflection, δ = –25° (right)

Different flow conditions were simulated using a relative wind vector parameterized by Mach number, roll angle (ϕ), and total angle of attack (α_T). An example of the relative wind vector is shown in Fig. 4.

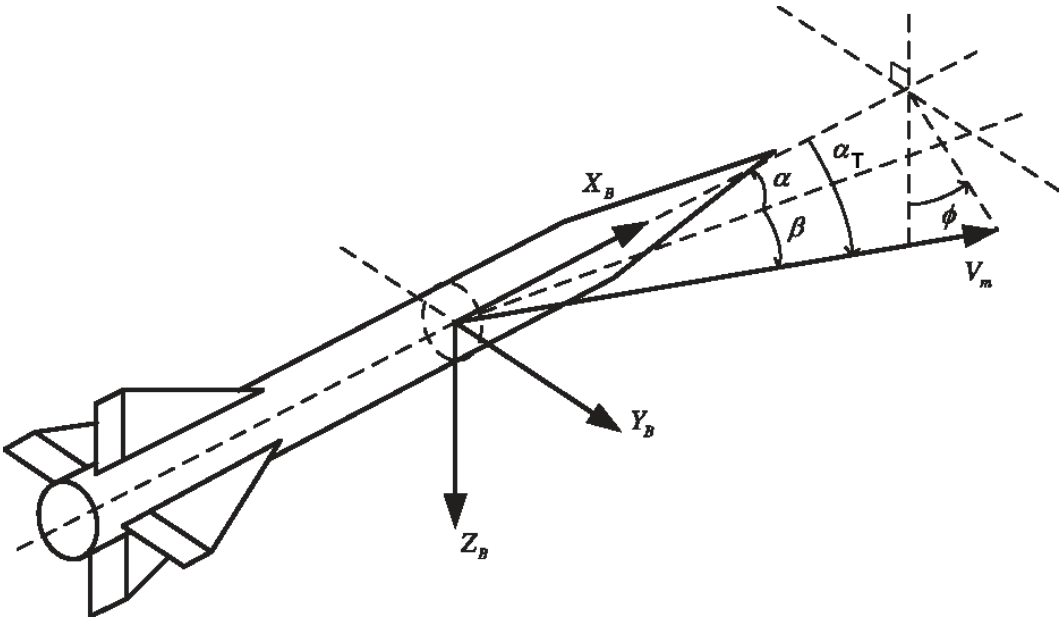

Fig. 4 Example of a relative wind vector for a generic projectile characterized by [α, β] or [α_T, ϕ]

Due to the construction and programming of Cart3D, roll angle and total angle of attack had to be converted into angle of attack (α) and beta (β) using the following equations:

$$\alpha = \tan^{-1}(\tan(\alpha_T) * \cos(\phi)) \quad (1)$$

$$\beta = \sin^{-1}(\sin(\alpha_T) * \sin(\phi)) \quad (2)$$

Including the flap deflection angle, the full simulation matrix of parameter values consists of 12 angles of attack, 15 deflections, 16 Mach numbers, and 32 bank angles. This simulation matrix yields a total quantity of 92,160. Due to this large number of simulations, an in-house Python driver system was used to automate job control and data logistics. The total project cost approximately 650,000 compute hours on the high-performance computing machine Onyx at the US Army Engineer Research and Development Center DOD Supercomputing Resource Center. Once the database was completed, a subset of the data was inspected via flow visualization. An example of this visualization is shown in Fig. 5, which contains Mach number contour slices of the flow superimposed with contours of pressure coefficient on the surface of the flight vehicle at Mach 2 with $\delta = 25°$, $\alpha_T = 20°$, and $\phi = 180°$.

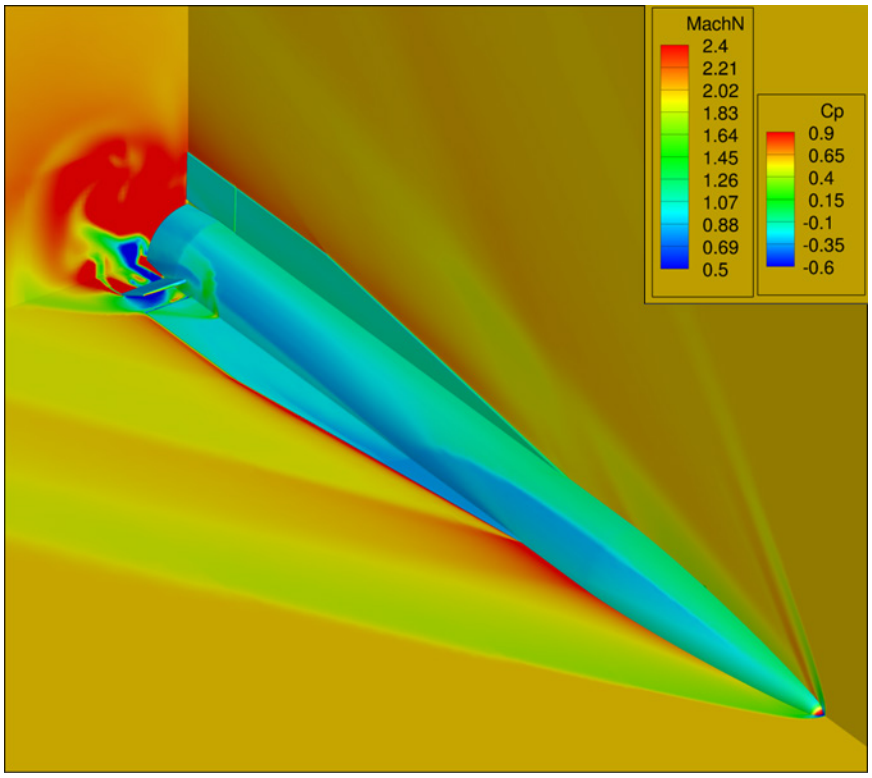

Fig. 5 Contour of Mach number and surface pressure coefficient simulated at Mach 2 with $\delta = 25°$, $\alpha_T = 20°$, and $\phi = 180°$

3. Method: Fourier Series Interpolation and Superposition

Previous studies have approximated the roll-dependent aerodynamics as a single harmonic with period assumed to be 2π divided by the number of fins.[1–4] However, large angle-of-attack studies in CFD indicate that additional harmonics are required to fully capture the behavior of moment and force components. Also, since the projectile has periodic symmetry, harmonic basis functions are a logical choice to properly interpret the CFD output along the roll direction.

3.1 The Complex Valued Fourier Series

Any periodic function $f(t)$ with period T may be approximated by the finite series of harmonics

$$\hat{y} = X_0 + 2\sum_n |X_n| \cos(2\pi n \cdot \phi/T + \angle X_n) \tag{3}$$

where X_n is a complex number defined by

$$X_n = \frac{1}{T}\int_0^T f(t) e^{-\frac{2\pi n i t}{T}} dt \tag{4}$$

Considering the periodic symmetry of the projectile outer mold line, the period is assumed to be $T = \pi/2$ for rigid aero surfaces (body and strakes) and $T = 2\pi$ for moving aerodynamic surfaces, since they move independently. However, if the forces and moments are written in the body frame, the period for rigid aero surfaces will be $T = 2\pi$ also.

The results of CFD are discrete points representing a force or moment component at a specific Mach number, angle of attack, and aerodynamic roll. Equation 4 is applied to each of these, integrating along the roll axis. Due to the discrete nature of the data, trapezoidal integration (trapz) renders an exact solution to Eq. 4, where $f(t)$ is the input data and dt is the discretization (typically 11.25° for this project).

Figure 6 shows the CFD pitch moment estimates for the rigid aerodynamic surfaces at Mach 2 for a range of angles of attack. Some outliers have already been removed and replaced by interpolating adjacent points. The solid lines are the instances of Eq. 3 found at each angle of attack by applying Eq. 4 to the data. The solid lines provide a smooth interpolation of the data that exhibits the expected symmetry and null points at 90 and 270°.

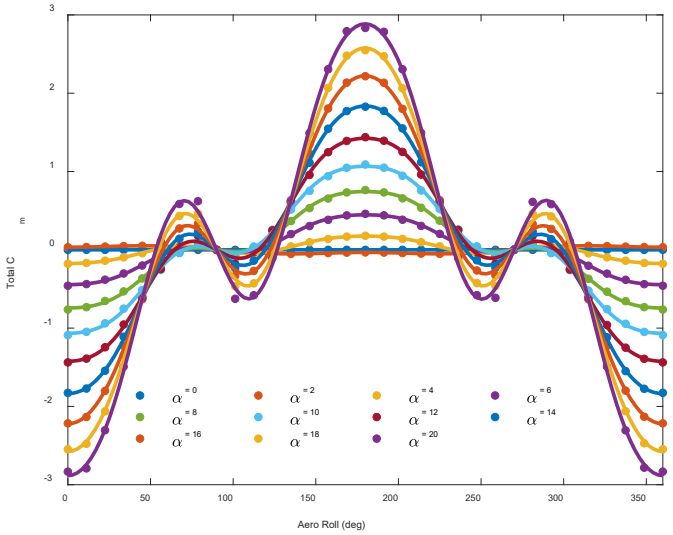

Fig. 6 Rigid aero surfaces, pitch moment CFD data at Mach 2 (dots). Fourier interpolation is superimposed (solid lines) showing smoothing, symmetry, and null points at phi-90, 270°.

3.2 Fourier Series by Direct Regression

Fourier series representation of a function may also be found by contriving the harmonic basis functions and solving for the amplitudes by regression. We found this method essential in order to model wind tunnel data where roll sweeps were performed for less than a full roll cycle. The method is based upon a rectangular version of the Fourier series such as

$$\hat{y} = \frac{a_0}{2} + \sum_{n=1}^{\infty} (a_n \cos 2\pi n \cdot \phi/T + b_n \sin 2\pi n \cdot \phi/T)$$

If $\hat{y} \approx f(\phi)$, the formula above may also be represented as a matrix multiplication:

$$\hat{y} = \frac{a_0}{2} \cdot \mathbf{1} +$$

$$\begin{bmatrix} \cos\left(\frac{2\pi\phi_1}{T}\right) & \cos\left(\frac{4\pi\phi_1}{T}\right) & \cdots & \sin\left(\frac{2\pi\phi_1}{T}\right) & \sin\left(\frac{4\pi\phi_1}{T}\right) & \cdots \\ \cos\left(\frac{2\pi\phi_2}{T}\right) & \cos\left(\frac{4\pi\phi_2}{T}\right) & \cdots & \sin\left(\frac{2\pi\phi_2}{T}\right) & \sin\left(\frac{4\pi\phi_2}{T}\right) & \cdots \\ \vdots & \vdots & \vdots & \vdots & \vdots & \ddots \end{bmatrix} \begin{Bmatrix} a_1 \\ a_2 \\ \vdots \\ b_1 \\ b_2 \\ \vdots \end{Bmatrix} \quad (5)$$

where $\mathbf{1}$ is a column vector of ones with length equal to that of ϕ. We may write more compactly:

$$\hat{y} = \frac{a_0}{2} \cdot \mathbf{1} + \mathbf{\Phi} \begin{Bmatrix} a_1 \\ a_2 \\ \vdots \\ b_1 \\ b_2 \\ \vdots \end{Bmatrix}$$

Thus, if we assume zero bias ($a_0 = 0$), the coefficients a_n, b_n may be found by a least-squares solution (regression) of Eq. 5. Bias may be included in the regression by appending $\mathbf{\Phi}$ with a column of ones and appending the parameter vector with unknown $a_0/2$. Conversion from the polar Fourier series (Eq. 3) to rectangular is explored in the Appendix.

3.3 Finding Polynomial Coefficients for a Dense Roll Grid

In order to find a mathematically tractable, yet precise model of the projectile aerodynamics, we chose to interpolate the total force and moment coefficients from CFD onto a finer roll grid. The CFD test matrix included the total force and moment coefficients for several Mach numbers and angles of attack, each swept a full roll cycle in increments of 11.25°. In order to maintain accuracy within the simulation while using linear interpolation, the Fourier series was used to smooth and interpolate each force/moment component along the roll direction. The result was a finer grid in bank at increments of 2.8125°. By using harmonic basis functions, smoothness, symmetry, and null values at certain angles of interest were ensured. Coefficients were then found at each bank angle such that the total force or moment coefficient was approximated by a high-order polynomial in α. Figure 7 illustrates the process using the total rigid aero surface pitch moment coefficient.

More specifically, Eqs. 3 and 4 were used to approximate each total force/moment coefficient for one angle of attack over a full roll cycle. Typically, three to six harmonics were required to fully capture the function profile observed in the CFD grid. Equation 3 was then used to predict the total force/moment coefficient over the finer roll grid (every 2.8125°) where the CFD grid was every 11.25°. This is interpolating along the "Aero Roll" axis in Fig. 7. The Fourier coefficients found at each Mach number, deflection, and AoA are also saved for later comparison with the wind tunnel data. At each bank angle in the fine grid, Eq. 3 was evaluated for 11 values of α ($\alpha \in \{0, 2, 4, \ldots, 20\}$) degrees. Given the total/force moment coefficient at this set of α, a polynomial regression is performed such that the force/moment coefficient at the given bank angle is approximated as

$$C_{\vartheta}^{R} = C_{\vartheta 0}^{R}(M,\phi) + C_{\vartheta 1}^{R}(M,\phi)\alpha + C_{\vartheta 2}^{R}(M,\phi)\alpha^2 + C_{\vartheta 3}^{R}(M,\phi)\alpha^3 + C_{\vartheta 4}^{R}(M,\phi)\alpha^4 + C_{\vartheta 5}^{R}(M,\phi)\alpha^5 \quad (6)$$

Thus, the regression is done along the α axis, resulting in 129 curves, such as the red stripe shown in Fig. 7; we show that each coefficient (for rigid aero surfaces) is a function of Mach and aerodynamic bank.

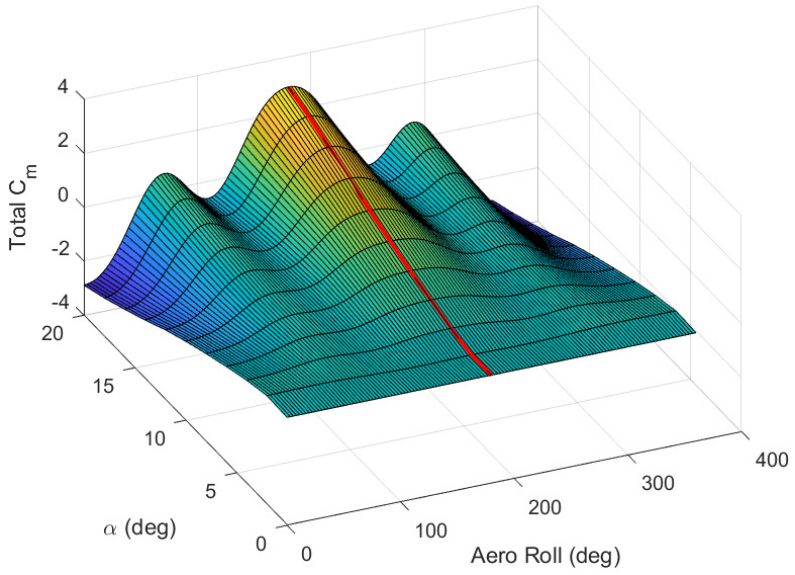

Fig. 7 Sample of interpolation and regression

The final tables are a comprehensive set of coefficients for 129 bank angles and 16 Mach numbers. For moving aero surfaces, each table has an additional dimension of deflection, so that, for instance, $C_{\vartheta i}^{M} = C_{\vartheta i}^{M}(M,\phi,\delta)$. About 15 deflection values are used in the current model.

3.4 Full Model Buildup by Superposition

Only the first flap or moving aerodynamic surface (MAS) was modeled in CFD. Assuming that all surfaces contribute equivalent force/moment terms for similar relative wind conditions, a full roll sweep of "MAS1" provides all the data needed to model the entire projectile with independently moveable flaps. Figure 8 illustrates the various frames needed to find the correct combination of terms for superposition.

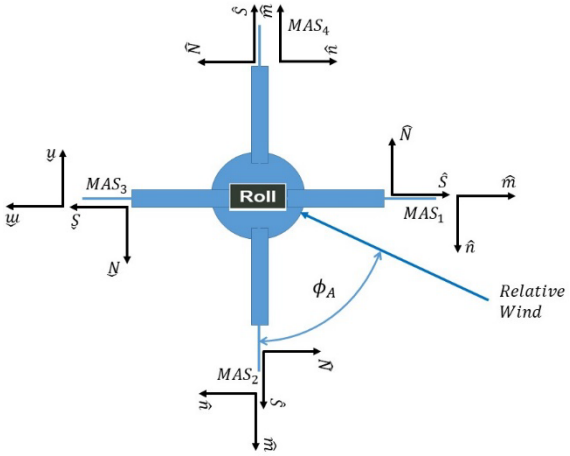

Fig. 8 Local frames for MAS buildup

First, note that aerodynamic bank is defined as the angle subtended from the body *Z* axis (MAS2) counterclockwise to the projection of relative wind on the y-z plane. Thus, moving clockwise from MAS1 to MAS2, the aerodynamic bank in the local MAS2 frame is the body aerodynamic bank plus $\pi/2$. Continuing to move around the projectile, the aerodynamic bank angle for each subsequent MAS is $\pi/2$ larger than the previous one. Specifically, this results in

$$C_S^{M_2}(\phi) = C_S^{M_1}\left(\phi + \frac{\pi}{2}\right), \quad C_S^{M_3}(\phi) = C_S^{M_1}(\phi + \pi), \tag{7a,b}$$

$$C_S^{M_4}(\phi) = C_S^{M_1}(\phi + 3\pi/2) \tag{7c}$$

$$C_N^{M_2}(\phi) = C_N^{M_1}\left(\phi + \frac{\pi}{2}\right), \quad C_N^{M_3}(\phi) = C_N^{M_1}(\phi + \pi), \tag{8a,b}$$

and

$$C_N^{M_4}(\phi) = C_N^{M_1}(\phi + 3\pi/2) \tag{8c}$$

as well as equivalent instances for $C_m^{M_i}$ and $C_n^{M_i}$.

$$C_m^{M_2}(\phi) = C_m^{M_1}\left(\phi + \frac{\pi}{2}\right), \quad C_m^{M_3}(\phi) = C_m^{M_1}(\phi + \pi), \tag{7d,e}$$

$$C_m^{M_4}(\phi) = C_m^{M_1}(\phi + 3\pi/2) \tag{7f}$$

$$C_n^{M_2}(\phi) = C_n^{M_1}\left(\phi + \frac{\pi}{2}\right), \quad C_n^{M_3}(\phi) = C_n^{M_1}(\phi + \pi), \tag{8d,e}$$

and

$$C_n^{M_4}(\phi) = C_n^{M_1}(\phi + 3\pi/2) \tag{8f}$$

Second, note the local frames shown for normal and side force components, and pitch and yaw moments (*m,n*). It is readily seen that the total transverse force contributions for the rigid aerodynamic surfaces (RAS) and all four MAS can be written in the body (*B*) or MAS1 frame as

$$C_S^B = C_S^R + C_S^{M_1} + C_N^{M_2} - C_S^{M_3} - C_N^{M_4} \tag{9}$$

and

$$C_N^B = C_N^R + C_N^{M_1} - C_S^{M_2} - C_N^{M_3} + C_S^{M_4} \tag{10}$$

Likewise, the transverse moment contributions are summed in the body frame by

$$C_m^B = C_m^R + C_m^{M_1} - C_n^{M_2} - C_m^{M_3} + C_n^{M_4} \tag{11}$$

and

$$C_n^B = C_n^R + C_n^{M_1} + C_m^{M_2} - C_n^{M_3} - C_m^{M_4} \tag{12}$$

Total force/moment coefficients were determined for the entire projectile with flaps set to zero deflection in two ways to validate the buildup. First, Cart 3D calculated total force/moment coefficients for the overall configuration. Second, Eqs. 7–12 were used to compute the total force/moment coefficients starting with the polynomial model of each component in its local frame. The two totals were compared for zero deflection, many Mach numbers, and angles of attack from 2° to 12°. Figure 9 contains sample plots for a typical comparison.

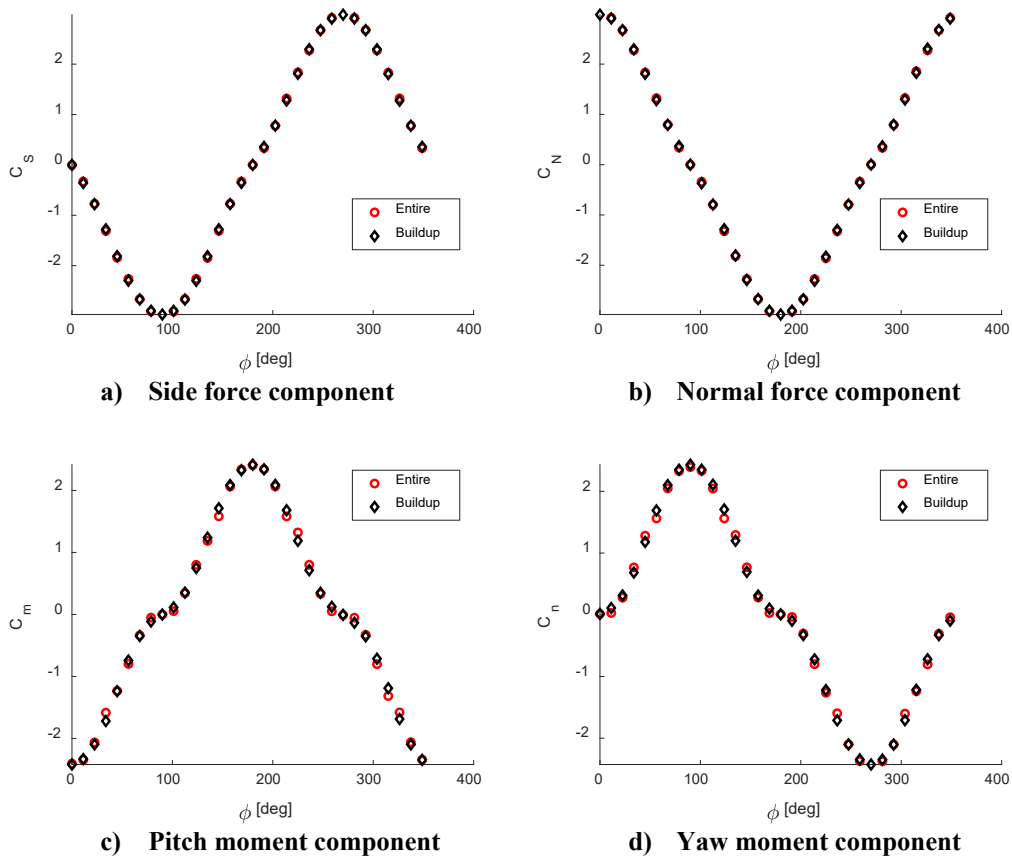

Fig. 9 Validating the superposition buildup. Sample results at Mach = 0.75, alpha = 12°. Red circles are taken directly from CFD. Black diamonds show the total after applying the polynomial model for each component, then totaling in the body frame.

Since many of the wind tunnel tests were performed in "X" mode, we will also need to perform the buildup using the X mode body frame. Figure 10 displays the local effector and body frames when defined in X mode at zero kinematic bank. Note that the body *z* axis points vertically down (opposite the depicted body normal force unit vector). Aerodynamic bank is now defined as the angle subtended counterclockwise from the body *z* axis to the relative wind. Thus, ϕ is reduced by pi/4 for X mode as opposed to "plus" mode.

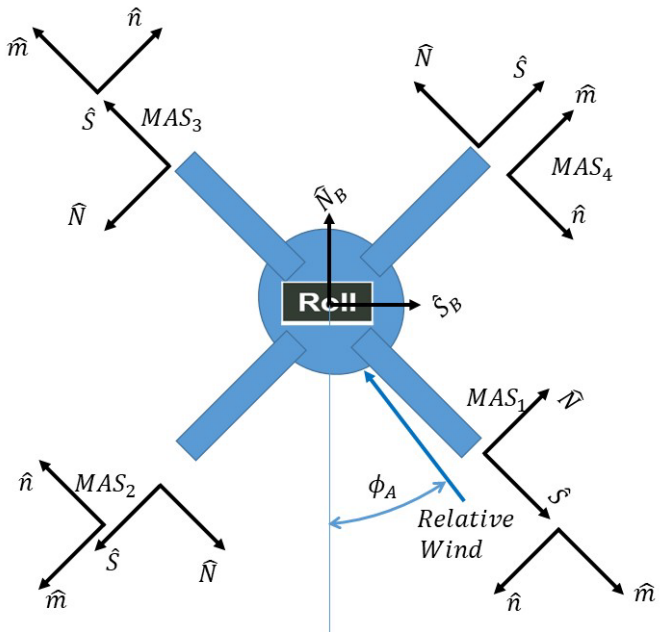

Fig. 10 Local frames for MAS buildup

Also, note that the MAS frames are no longer parallel or perpendicular to the body frame. Each set of MAS force/moment components will require a pi/4 rotation to body frame in addition to the component polarities defined in Eqs. 9–12. Specifically, if we define the rotation matrix

$$\mathbf{R} = \frac{\sqrt{2}}{2}\begin{bmatrix} 1 & 0 & 0 \\ 0 & 1 & -1 \\ 0 & 1 & 1 \end{bmatrix}$$

then each component of the force/moment buildup is rotated into alignment with the body vertical/horizontal frame by

$$\begin{Bmatrix} C_A \\ C_S \\ C_N \end{Bmatrix}^B = \mathbf{R}^T \begin{Bmatrix} C_A \\ C_S \\ C_N \end{Bmatrix}^L \tag{13}$$

for forces and

$$\begin{Bmatrix} C_l \\ C_m \\ C_n \end{Bmatrix}^B = \mathbf{R} \begin{Bmatrix} C_l \\ C_m \\ C_n \end{Bmatrix}^L \tag{14}$$

for moments, where the superscript L takes on all values $L \in \{R \quad M_1 \quad M_2 \quad M_3 \quad M_4\}$. After applying Eqs. 13 and 14 to the five components, the totals in the body frame require summation as defined in

Eqs. 9–12. Or, one could combine Eqs. 13, 14, and 9–12 to determine the full set of rotations from local effector frames to the body frame such as

$$\begin{Bmatrix} C_A \\ C_S \\ C_N \end{Bmatrix}^B_{\text{tot}} = \mathbf{R}^T \left(\begin{Bmatrix} C_A \\ C_S \\ C_N \end{Bmatrix}^R + \begin{Bmatrix} C_A \\ C_S \\ C_N \end{Bmatrix}^{M_1} + \begin{bmatrix} 1 & 0 & 0 \\ 0 & 0 & 1 \\ 0 & -1 & 0 \end{bmatrix} \begin{Bmatrix} C_A \\ C_S \\ C_N \end{Bmatrix}^{M_2} + \begin{Bmatrix} C_A \\ -C_S \\ -C_N \end{Bmatrix}^{M_3} + \begin{bmatrix} 1 & 0 & 0 \\ 0 & 0 & -1 \\ 0 & 1 & 0 \end{bmatrix} \begin{Bmatrix} C_A \\ C_S \\ C_N \end{Bmatrix}^{M_4} \right) \tag{15}$$

and

$$\begin{Bmatrix} C_l \\ C_m \\ C_n \end{Bmatrix}^{\text{B}}_{\text{tot}} = \mathbf{R} \left(\begin{Bmatrix} C_l \\ C_m \\ C_n \end{Bmatrix}^R + \begin{Bmatrix} C_l \\ C_m \\ C_n \end{Bmatrix}^{M_1} + \begin{bmatrix} 1 & 0 & 0 \\ 0 & 0 & -1 \\ 0 & 1 & 0 \end{bmatrix} \begin{Bmatrix} C_l \\ C_m \\ C_n \end{Bmatrix}^{M_2} + \begin{Bmatrix} C_l \\ -C_m \\ -C_n \end{Bmatrix}^{M_3} + \begin{bmatrix} 1 & 0 & 0 \\ 0 & 0 & 1 \\ 0 & -1 & 0 \end{bmatrix} \begin{Bmatrix} C_l \\ C_m \\ C_n \end{Bmatrix}^{M_4} \right) \tag{16}$$

since the 45° rotation applies uniformly to all components.

4. Wind Tunnel Validation

Total force/moment components were measured using a one-fifth subscale model at the Florida State University wind tunnel.[9] Aerodynamic roll was varied from –90° to +90° by rotating the model in a constant pitch orientation. Zero degree aerodynamic roll was defined as the "X" configuration. Angle of attack was held constant at approximately 12°. Mach was varied within the set

$$Mach \in \{0.4, 0.5, 0.6, 0.7, 0.8, 0.9, 1.1, 1.2, 2, 4, 5\}$$

Since the sting has a constant orientation with respect to the flow, force and moment components are measured in a "fixed plane" system. In order to compare with the model of Eqs. 7–16, the wind tunnel results were rotated into the body frame. The coefficient tables created for Eq. 6 define zero aerodynamic roll to be the "+" configuration, so a 45° bias was subtracted from roll before table lookups.

4.1 Direct Comparisons

As a first check, the aerodynamic model was compared with roll sweeps from the wind tunnel data. The wind tunnel model provides total force/moment coefficients for the entire assembly in a fixed-plane (tunnel) frame. Thus, in order to compare with the aero model, the wind tunnel data will need to be rotated into the body

frame by removing the aerodynamic roll. This can be done by defining the rotation matrix in terms of the aerodynamic roll (ϕ):

$$\mathbf{R} = \begin{bmatrix} 1 & 0 & 0 \\ 0 & c_\phi & s_\phi \\ 0 & -s_\phi & c_\phi \end{bmatrix}$$

Then, the wind tunnel force coefficients are transformed into the body frame by

$$\begin{Bmatrix} C_A \\ C_S \\ C_N \end{Bmatrix}^B = \mathbf{R}^T \begin{Bmatrix} C_A \\ C_S \\ C_N \end{Bmatrix}^{WT} \tag{17}$$

and the moment components by

$$\begin{Bmatrix} C_l \\ C_m \\ C_n \end{Bmatrix}^B = \mathbf{R} \begin{Bmatrix} C_l \\ C_m \\ C_n \end{Bmatrix}^{WT} \tag{18}$$

Figure 11 shows a sample comparison between wind tunnel (WT) data and aero model (AM) prediction. Results are shown for Mach 0.7. Note the excellent match in the force coefficients. At least two harmonics are evident in both curves with good agreement for the entire range plotted.

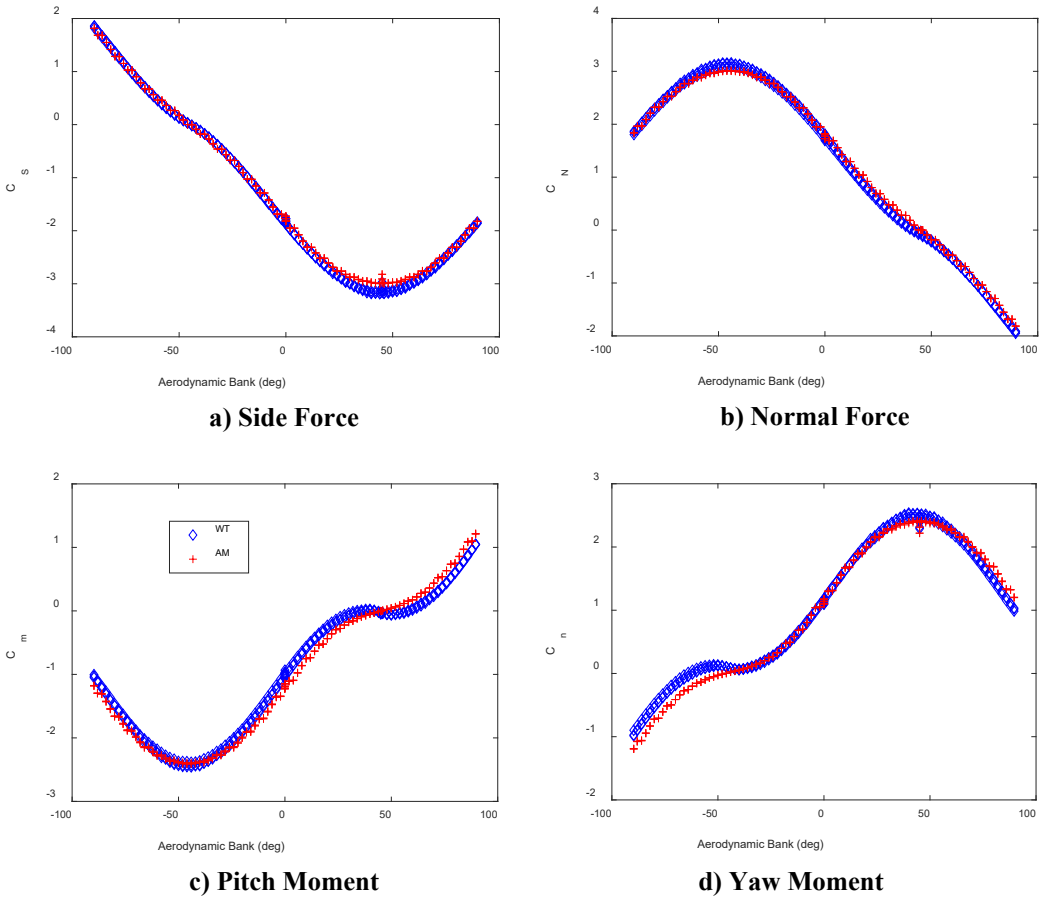

Fig. 11 Sample comparison between wind tunnel (WT) and aero model (AM), in body frame, roll sweep, AoA = 12°, Mach = 0.7, zero deflections

In Figures 12–15, we plot the transverse force and moment coefficients from roll sweeps for the wind tunnel and aero model predictions. This allows us to confirm that the frame transformations in Eqs. 8–11 and 17–18 are correct.

Wind tunnel roll sweeps were performed from –90° to +90° of aerodynamic bank, where phi = 0 is defined as the X configuration. The aero model predictions are aligned accordingly along the bank axis. In all cases (13–16), the aero model matches the wind tunnel transverse force coefficients very closely. Note also that the normal force component (C_N) has a null point at +45° of bank. Likewise, the side force component (C_S) has a node at –45° of bank.

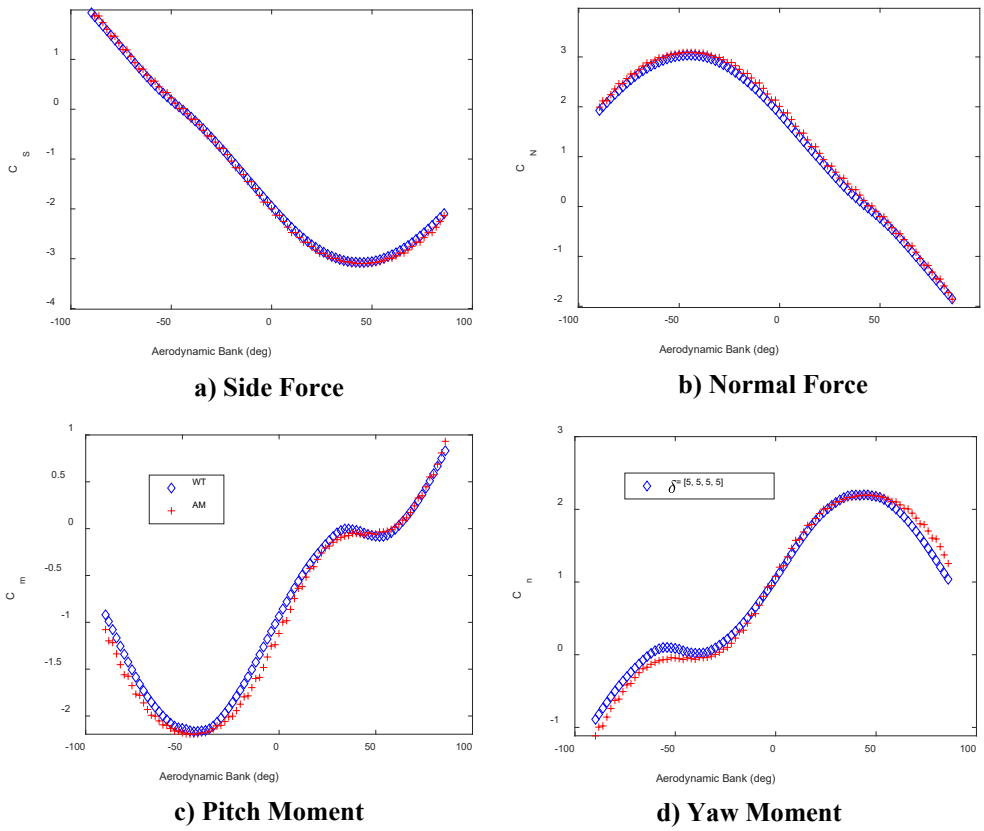

Fig. 12 Sample comparison between wind tunnel (WT) and aero model (AM), in body frame, roll sweep, AoA = 12°, Mach = 0.7, δ = [5 5 5 5]

The aero model consistently overpredicts the pitch and yaw moment coefficients. This is especially evident in each pitch plot near 0° of bank and in each yaw plot near –90° and +90° of bank.

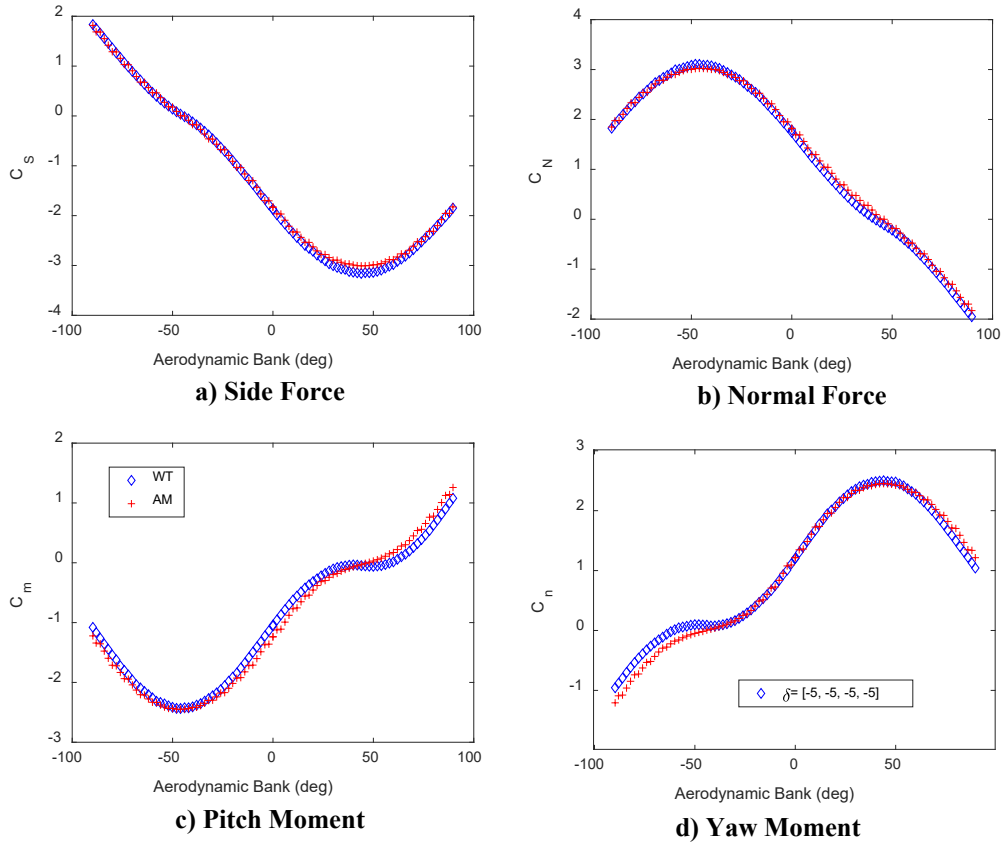

Fig. 13 Sample comparison between wind tunnel (WT) and aero model (AM), in body frame, roll sweep, AoA = 12°, Mach = 0.7, $\delta = [-5 \quad -5 \quad -5 \quad -5]$

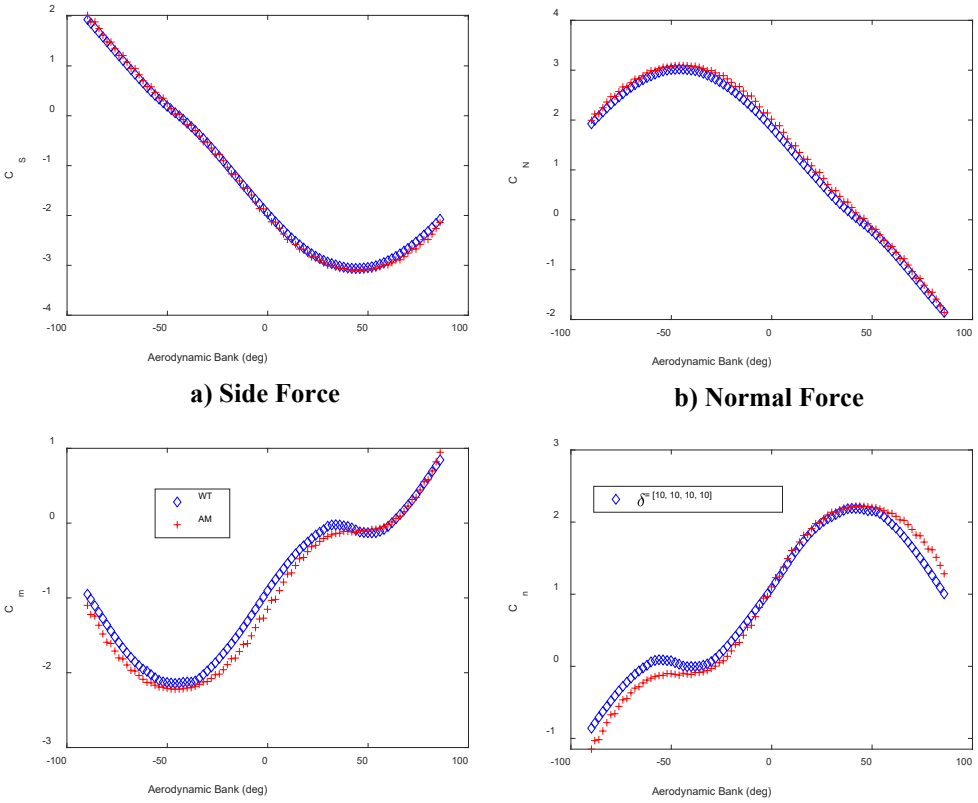

a) Side Force **b) Normal Force**

c) Pitch Moment **d) Yaw Moment**

Fig. 14 Sample comparison between wind tunnel (WT) and aero model (AM), in body frame, roll sweep, AoA = 12°, Mach = 0.7, δ = [10 10 10 10]

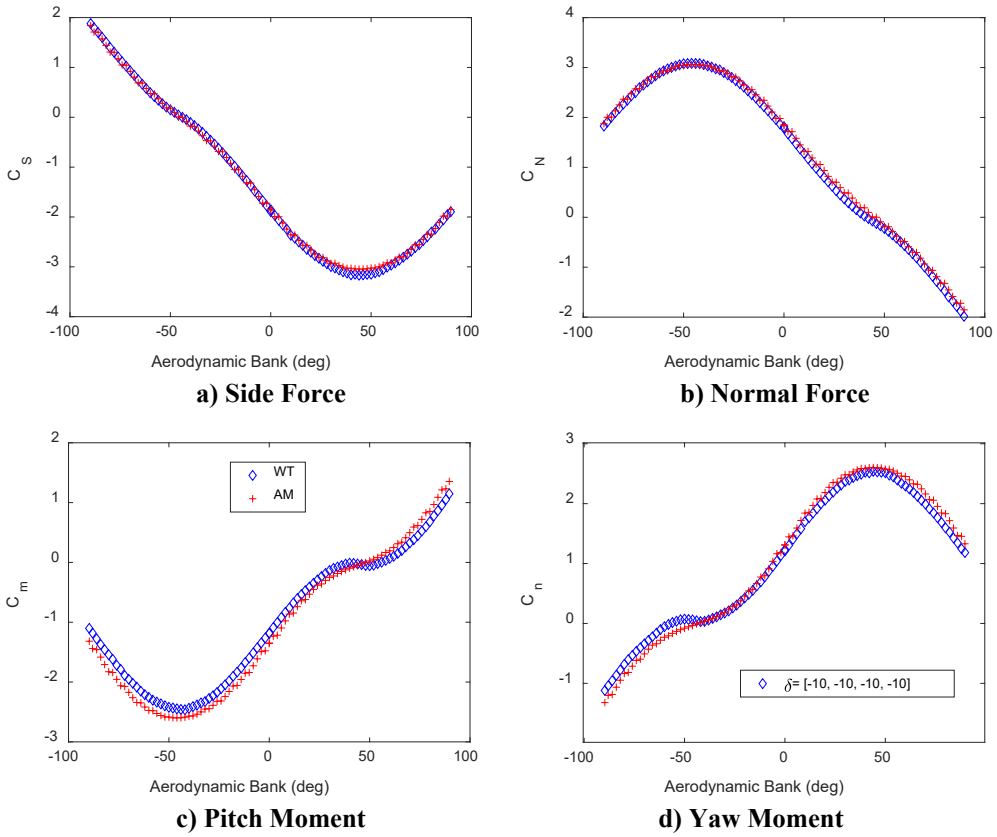

Fig. 15 Sample comparison between wind tunnel (WT) and aero model (AM), in body frame, roll sweep, AoA = 12°, Mach = 0.7, δ = $[-10 \quad -10 \quad -10 \quad -10]$

The wind tunnel experiments also included configurations with the flaps deflected in specific ways to induce pitch moments without inducing roll or yaw. These configurations were designed for flight in both the plus and X roll orientations. A portion of the wind tunnel test matrix illustrating these configurations is shown as Table 1. These wind tunnel tests did not include roll sweeps but did include angle-of-attack sweeps.

Table 1 Wind tunnel test conditions (courtesy of Florida State University)

Model	Deflections	Mach number	Pitch/roll sweeps
Baseline	0	0.4, 0.5, 0.6, 0.8, 0.9, 1.1, 1.2, 5	Pitch: 0° to 12° at Phi = 0° Pitch: 0° to 12° at Phi = 45° Roll: –90° to 90° at Alpha = 12° Roll: –90° to 90° at Alpha = 6°
	0	3, 5	Pitch: 0° to 12° at Phi = 0° Pitch: 0° to 12° at Phi = 45° Roll: –90° to 90° at Alpha = 12° Roll: –90° to 90° at Alpha = 6° Roll: 90° to –90° at Alpha = 0°
	0	2	Roll: –90° to 90° at Alpha = 10° Roll: –90° to 90° at Alpha = 4°
	0	0.7, 2	Pitch: 0° to 12° at Phi = 0° Pitch: 0° to 12° at Phi = 45° Roll: –90° to 90° at Alpha = 12° Roll: –90° to 90° at Alpha = 6° Roll: 90° to –90° at Alpha = 0°
Deflected	+ El – El	0.7, 2	Pitch: 0° to 12° at Phi = 0° Pitch: 0° to 12° at Phi = 45°
	+ Ail – Ail	0.7, 2	Roll: –90° to 90° at Alpha = 12° Roll: –90° to 90° at Alpha = 6° Roll: 90° to –90° at Alpha = 0°

Figure 16 shows the result at Mach 2 in plus mode with a 5° pitch deflection. Note that aero model normal force predictions are very accurate for the entire range. The aero model was contrived to predict null values of side force and side moment at 0° of bank. This is reflected well in Fig. 16a and d. However, the wind tunnel captured small but negligible amounts of side force and side moment at most angles of attack, perhaps due to the bank angle not being set to exactly zero. The pitch moment matches well at zero angle of attack but diverges for larger angles of attack.

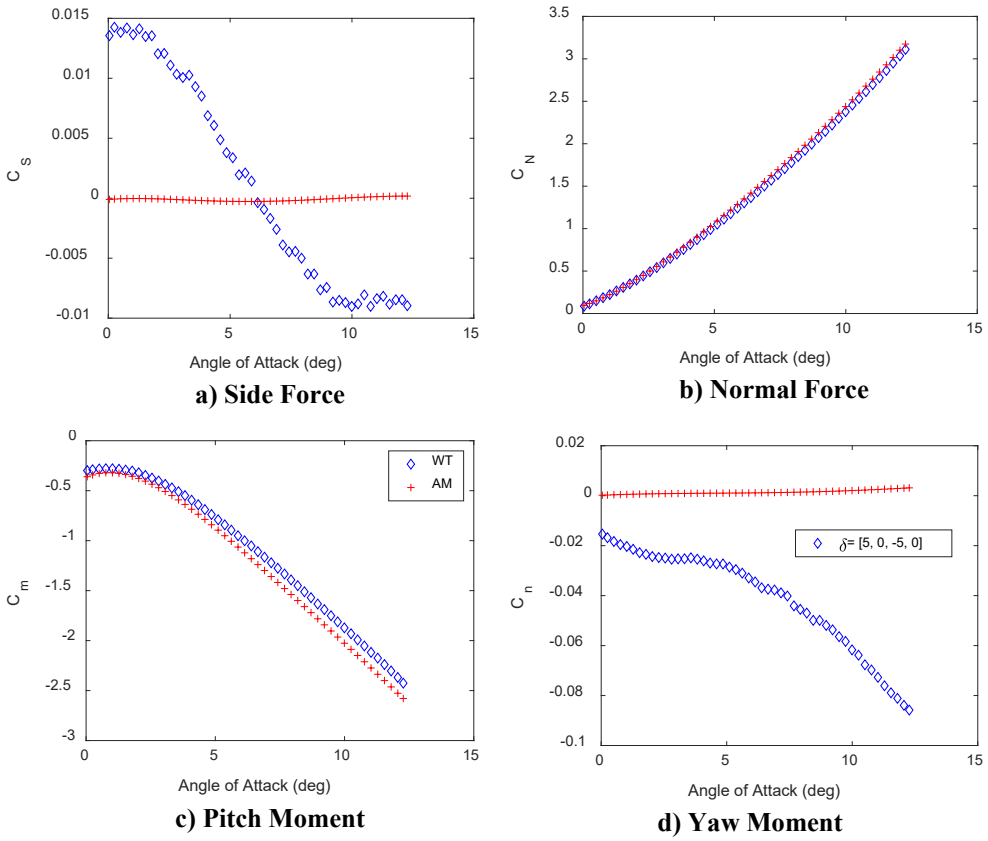

Fig. 16 Comparison between wind tunnel (WT) and aero model (AM), in body frame, AoA sweep, Mach = 2.0, plus mode, $\delta = [5 \quad 0 \quad -5 \quad 0]$

For Fig. 17, the pitch deflection is doubled. The largest apparent difference from the 5° deflection case is in the pitch moment bias. In Fig. 16, the zero angle-of-attack pitch moment was above –0.5. In Fig. 17, it has reached nearly –1.0 due to the added deflection. The rest of the pitch moment profile is largely unchanged, indicating that angle of attack has a stronger influence than deflection as angle of attack in increased.

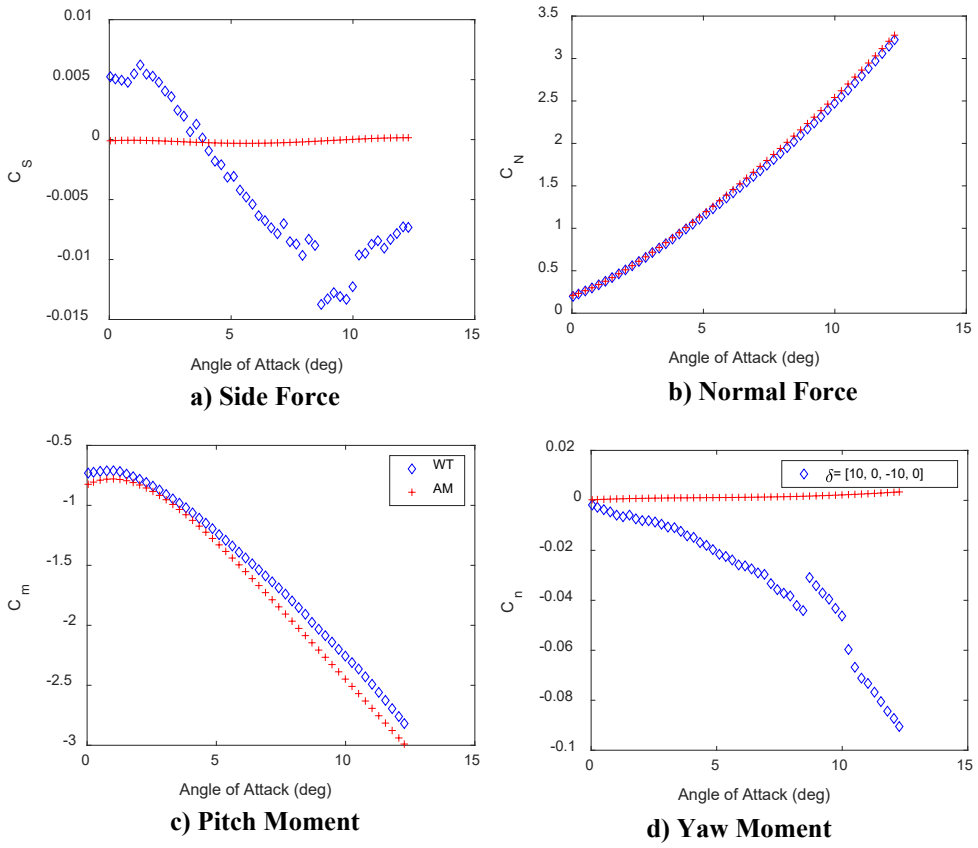

Fig. 17 Comparison between wind tunnel (WT) and aero model (AM), in body frame, AoA sweep, Mach = 2.0, plus mode, $\boldsymbol{\delta} = [10 \quad 0 \quad -10 \quad 0]$

In Figs. 18, 19, and 20, we have repeated the comparison for pitch deflections in X mode. At 5° pitch deflection (Fig 18), the normal force and pitch moment coefficients match well in bias as well as in nonzero angle-of-attack cases. Doubling the deflection to 10° (Fig. 19), a significant difference in bias is observed. The normal force and pitch moment curves are otherwise parallel, indicating that the only significant error is in the bias terms for pitch moment and normal force. As we double the deflection again (Fig. 20), the bias error increases, but the pitch moment and normal force curves remain parallel. Thus, the aero model predictions differ from the wind tunnel primarily in the bias term. We explore tuning the aero model to the wind tunnel data later in this report.

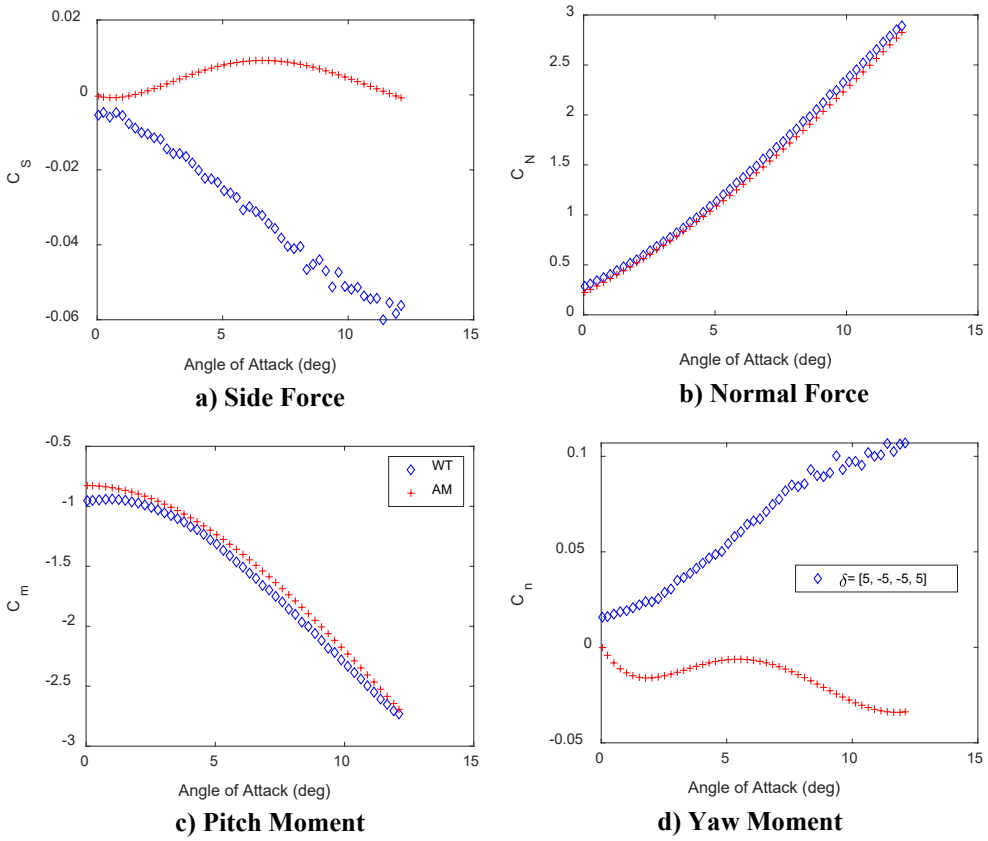

Fig. 18 Comparison between wind tunnel (WT) and aero model (AM), in body frame, AoA sweep, Mach = 0.7, X mode, $\delta = [5 \quad 5 \quad -5 \quad -5]$

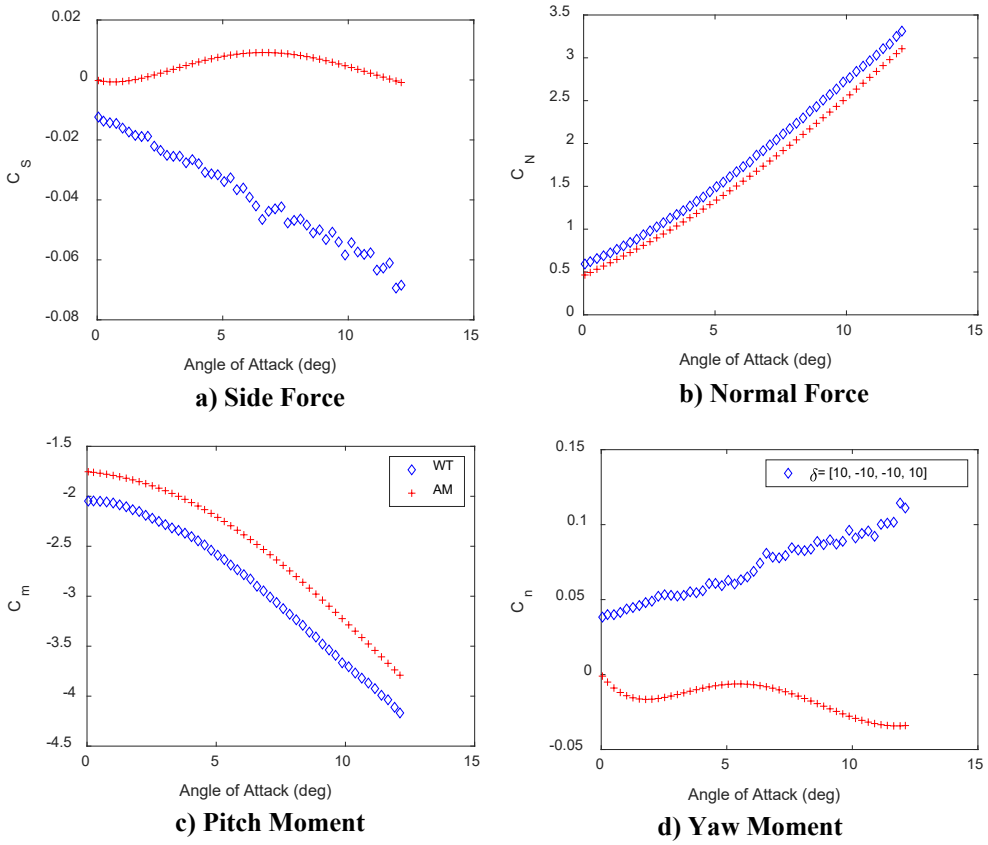

Fig. 19 Comparison between wind tunnel (WT) and aero model (AM), in body frame, AoA sweep, Mach = 0.7, X mode, $\delta = [10 \quad 10 \quad -10 \quad -10]$

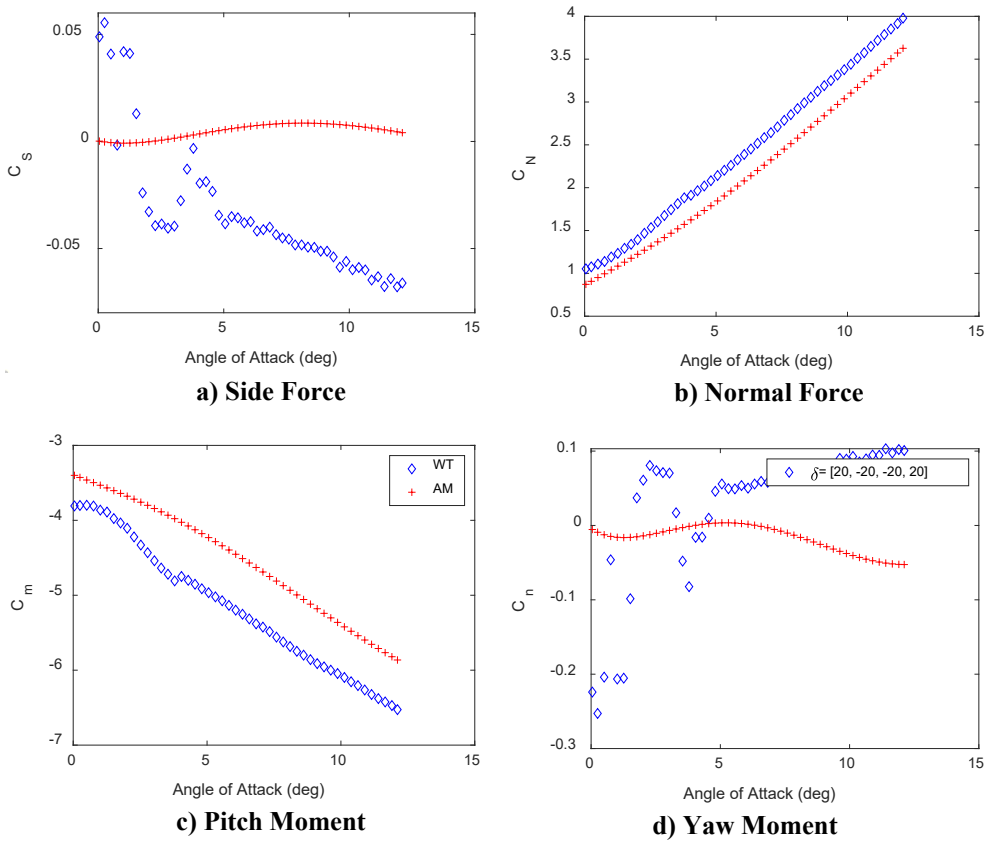

Fig. 20 Comparison between wind tunnel (WT) and aero model (AM), in body frame, AoA sweep, Mach = 0.7, X mode, $\boldsymbol{\delta = [20 \quad 20 \quad -20 \quad -20]}$

4.2 Neural Net Tuning of the Fourier Model

Combining the methods presented in Eqs. 8–11, and Eq. 5, an alternative model can be built in the form of a Widrow–Hoff (linear feedforward) neural network. This network will predict the transverse forces and moments for the entire projectile based upon the Cartesian Fourier representation. By comparing the model prediction with the Fourier model found from wind tunnel data by direct regression, the Fourier model coefficients may be tuned using a steepest descent algorithm.

We demonstrate the method here and present some sample results. Equation 5 may be applied to forces and moments from either an individual component of the projectile (RAS, MAS1, etc.), such as in the preceding reduction of Cart3D data, or to the entire projectile, such as the wind tunnel measurements. Thus, given a set of Fourier coefficients for an individual component (a_n, b_n), one could predict a force or moment contribution in the local frame of that component. By expanding Eq. 5 slightly,

$$\hat{\mathbf{y}} = \mathbf{\Phi}\begin{Bmatrix} a_1^S & a_1^N \\ a_2^S & a_2^N \\ \vdots & \vdots \\ b_1^S & b_1^N \\ b_2^S & b_2^N \\ \vdots & \vdots \end{Bmatrix} = \mathbf{\Phi} \cdot \mathbf{\Xi} \tag{19}$$

We can predict both components of transverse force (C_S, C_N) in a single matrix multiplication in the local frame. Equations 8–11 or 12–15 may be achieved by two more matrix multiplications in series. By transposing Eq. 19, $\hat{\mathbf{y}}$ becomes two long rows representing the force components over a partial roll cycle. Thus, premultiplying by a 45° rotation (Eqs. 12–13 if X mode is desired), and then by a 90° rotation (shown by the binary matrices that multiply MAS terms in Eqs. 14–15), the force predictions may be transformed into the desired body frame. In one equation, this is

$$\hat{\mathbf{y}}^B = \mathbf{R} \cdot \mathbf{R}_{\mathbf{90^\circ}} \cdot (\mathbf{\Phi} \cdot \mathbf{\Xi})^{\boldsymbol{T}} \tag{20}$$

where $\mathbf{R}$ was previously defined and $\mathbf{R}_{\mathbf{90^\circ}}$ takes on one of four values depending on which component (RAS, MAS*i*) is being predicted.

$$\mathbf{R}_{\mathbf{90^\circ}} = \mathbf{I}, \quad \mathbf{R}_{\mathbf{90^\circ}} = -\mathbf{I}$$

$$\mathbf{R}_{\mathbf{90^\circ}} = \begin{bmatrix} \mathbf{0} & \mathbf{1} \\ \mathbf{-1} & \mathbf{0} \end{bmatrix} \text{ or } \mathbf{R}_{\mathbf{90^\circ}} = \begin{bmatrix} \mathbf{0} & \mathbf{-1} \\ \mathbf{1} & \mathbf{0} \end{bmatrix}$$

In order to build up a prediction for the entire projectile, an instance of Eq. 20 is evaluated for each component, choosing the corresponding $\mathbf{R}_{\mathbf{90^\circ}}$. Force and moment coefficients for the entire vehicle can then be predicted by a simple sum.

If Eq. 20 is seen as forward propagation through a linear feedforward network, then the sensitivity of the prediction with respect to the parameters ($\mathbf{\Xi}$) can likewise be written as a backpropagation:

$$\frac{\partial \hat{\mathbf{y}}^B}{\partial \mathbf{\Xi}} =\cdot \mathbf{R}_{\mathbf{90^\circ}}^T \cdot \mathbf{R}^T \cdot (\mathbf{1} \cdot \mathbf{\Phi}) \tag{21}$$

Premultiplying by $\mathbf{R}^T$ results in a row of zeros in the sensitivities, so comparisons must be done in the "plus" body frame, and we hold $\mathbf{R}^T = \mathbf{I}$. For practical implementation, only one row of $\mathbf{\Phi}$, and hence Eq. 21, is evaluated at a time, thus each row is treated as the sensitivity for one "training pair". The length two-column vector, $\mathbf{1}$, replicates that row of $\mathbf{\Phi}$ such that Eq. 21 renders a $2 \times 2n$ array of sensitivities, one row for each transverse force component and a column for each a_n, b_n. Each of these sensitivities is then used to populate a Jacobian matrix. We use separate Jacobians for each force and moment component.

Meanwhile, we apply Eq. 5 to the actual wind tunnel data of the entire projectile in order to smooth the data. The resulting Fourier *model* is then compared to the network predictions in order to tune the network. Separate residuals and Jacobians are found for each force/moment component. Thus, the tuning algorithm resembles Widrow–Hoff as subsets of the coefficients are tuned sequentially based upon subsets of the system gradient.

4.3 Rigid Aero Surface Terms

Since roll cycle data was only available for configurations where all flap deflections were set to equal values (roll deflections), the tuning algorithm shown previously was applied to only the rigid aero surface predictions in order to match these data sets. Equal flap deflections approximately cancel each other out in pitch and yaw, so tuning the MAS for such data would be ill-conditioned, hindering convergence.

Figure 21 compares the wind tunnel data, three-term Fourier model from direct regression of wind tunnel data, Fourier model from Cart3D as described in Section 3.1, and Fourier model found from network tuning of the Fourier model found in Section 3.3. The comparison is done in the plus mode body frame—wind tunnel measurements had to be rolled into this frame. The yellow line is a three-term Fourier approximation to the actual data, which fits in a least squares sense. The "Fourier tuned AM" was trained using the Fourier model of the wind tunnel data as truth. After the three steepest descent steps, the model predictions of all four force/moment components fit with a residual whose two-norm is less than 10^{-13}.

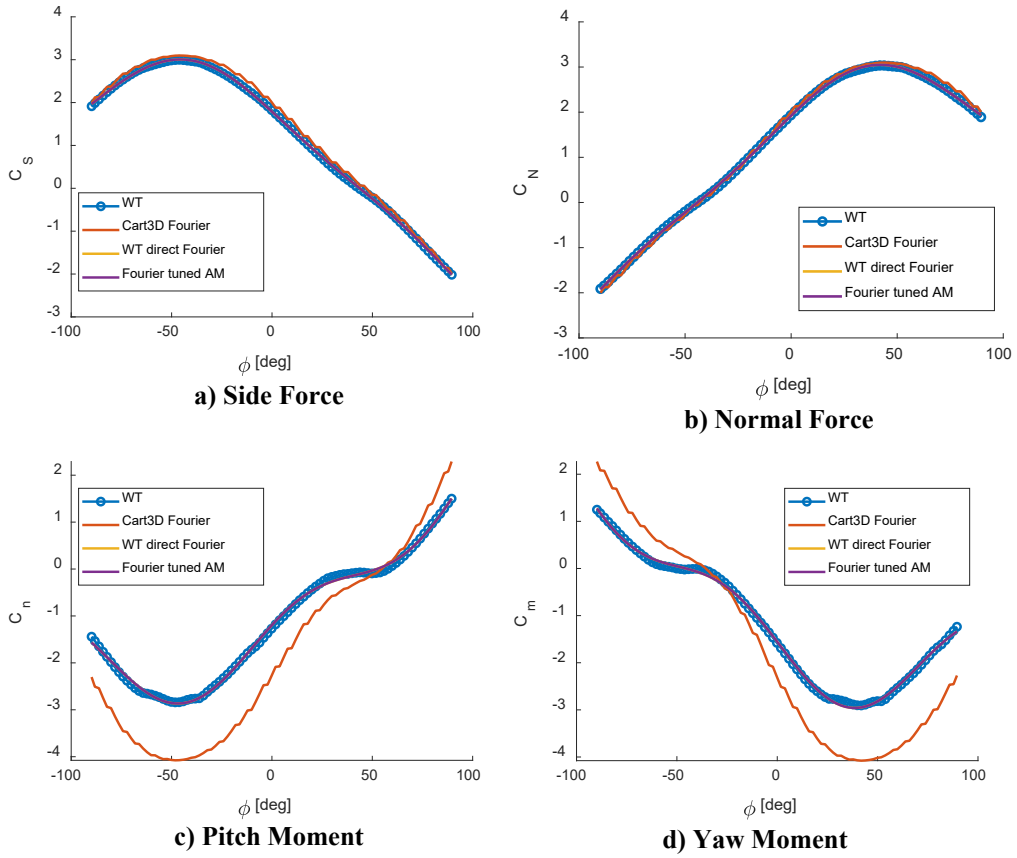

Fig. 21 Comparison between wind tunnel (WT) and tuned aero model (AM), in body frame, roll sweep, Mach = 2.0, plus mode, $\boldsymbol{\delta} = [\mathbf{20} \quad \mathbf{20} \quad \mathbf{20} \quad \mathbf{20}]$

Figure 22 compares the Fourier coefficients after tuning to those found using the method of Section 3.3. The blue squares represent the Fourier coefficients found from Cart3D using the method of Section 3.1 and converted to Cartesian form. The red diamonds are the same coefficients after tuning to the wind tunnel–based Fourier model. The top graph shows only small adjustments, reflecting the proximity of the untuned Fourier (red curves in Fig. 21a and b) and the wind tunnel data. Force components converge within 10^{-4} in the first steepest descent step. Since the moment predictions include a component due to the distance from center of gravity to center of pressure, the moment parameters lag in convergence by one step, reaching residuals less than 10^{-13} by the third step.

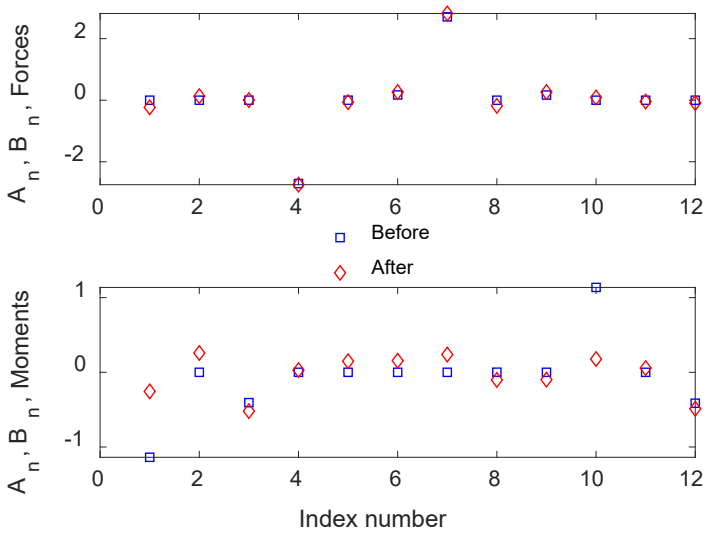

Fig. 22 Comparison of Fourier coeffcieints for rigid aero surface model from Cart3D before and after tuning to wind tunnel data. Mach = 2.0, plus mode, $\boldsymbol{\delta} = [\mathbf{20} \quad \mathbf{20} \quad \mathbf{20} \quad \mathbf{20}]$.

A second example will further illustrate the power of this method. Here we intentionally seed the algorithm with the Fourier coefficients for the model in the plus mode body frame. However, we provide the training data in the X mode body frame. Thus, the network model starts with the predictions shown as red curves in Fig. 21. Training data is shown in Fig. 23 as yellow curves, and the trained network predictions as purple curves. Initial residuals are thus considerably larger than the previous example. However, after only three iterations, all residuals are reduced to less than 10^{-13}, and the tuned model matches the training data exactly. The untuned Cart3D Fourier model is shown as a red curve in Fig. 23 to show its fidelity prior to tuning; however, this data is ignored in the actual tuning.

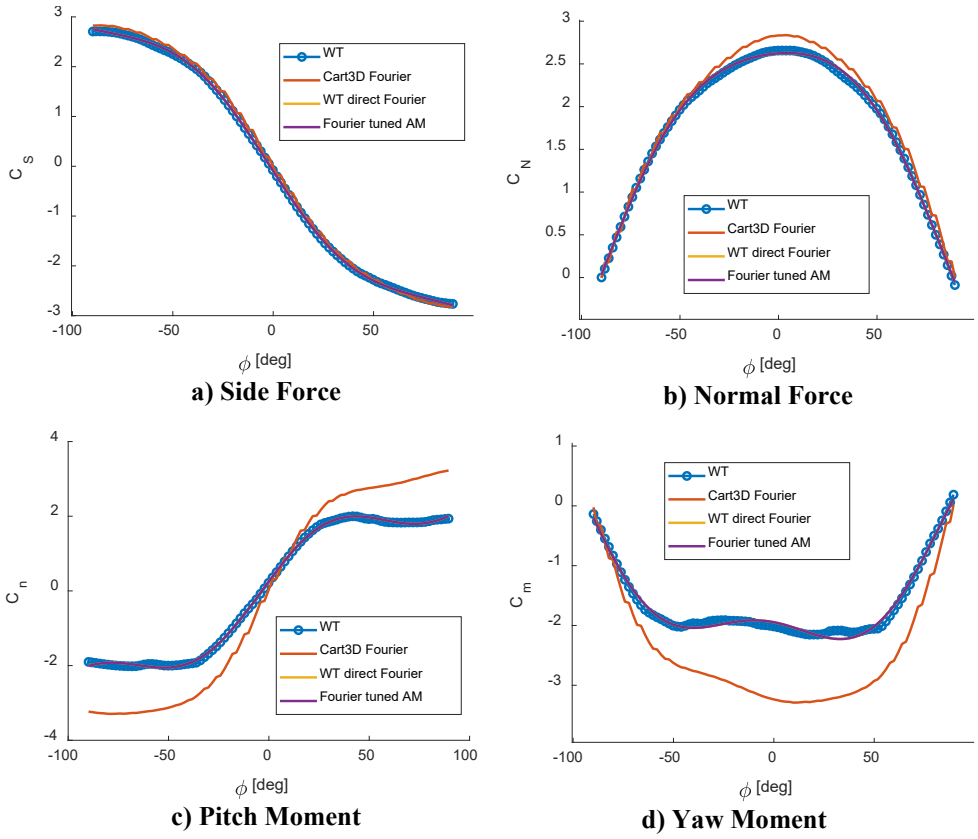

Fig. 23 Comparison between wind tunnel (WT) and tuned aero model (AM), in body frame, roll sweep, Mach = 2.0, X mode, algorithm seeded with plus mode Fourier predictions, $\boldsymbol{\delta = [20 \quad 20 \quad 20 \quad 20]}$

Figure 24 shows the Fourier coefficients for the untuned plus mode model as blue squares. Coefficients of the fundamental harmonics (a_1, b_1) are found at indices 1 and 4 for C_S and C_N and at indices 7 and 10 for C_m and C_n, respectively. Note that these coefficients move the most during tuning to adjust for the 45° phase difference moving from plus to X mode. Movement of the higher harmonics is not as apparent due to their smaller overall magnitudes.

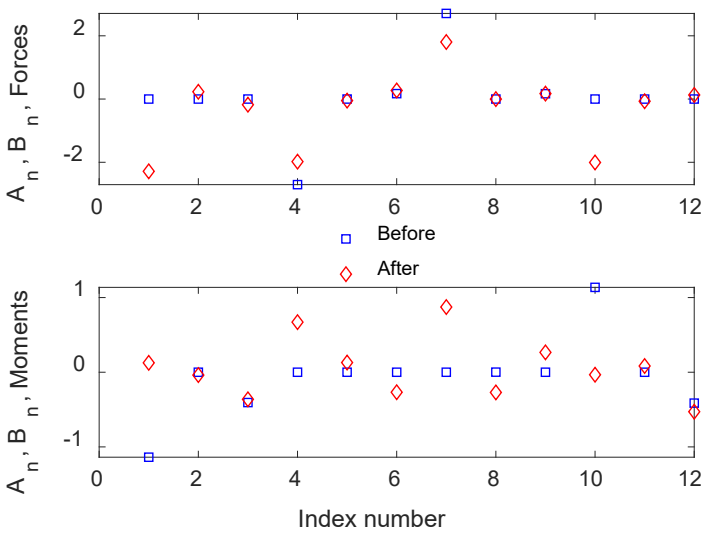

Fig. 24 Comparison of Fourier coefficients for Rigid Aero Surface Model from Cart3D before and after tuning to wind tunnel data. Mach = 2.0, plus mode, $\boldsymbol{\delta} = [\mathbf{20} \quad \mathbf{20} \quad \mathbf{20} \quad \mathbf{20}]$.

4. Conclusion

The aerodynamics of a long-range, high-speed projectile were modeled by exercising an inviscid CFD solver over a large test matrix. To convert the table of predictions from CFD into a format suitable for high-fidelity simulation, a multistep approach was performed. Obvious outliers were discarded and replaced through linear interpolation of adjacent points when possible. If consecutive points in the roll cycle were determined to be outliers, they were all replaced with values from the next lowest Mach number. At each Mach number and angle of attack, a Fourier series approximation to the data was found and used to smooth the input data, and interpolated to provide additional estimates every 2.8125° of bank. The predictions from Fourier were assembled at each bank angle for angles of attack from zero to 20°. These predictions were used in a regression to coefficients of up to a fifth-order polynomial in sin(α). Unique coefficients were found at each bank angle and Mach number. The process was repeated for a single deflected flap resulting in a table of coefficients as functions of bank, Mach number, and flap deflections. In order to validate the process and resulting model, the total transverse force/moment coefficients were built up for various configurations and Mach numbers and compared to both CFD predictions for the entire airframe, and wind tunnel measurements from a one-fifth scale model. The model compared well at all conditions predicted, with better performance in force prediction as opposed to moment prediction. A subsequent report will discuss tuning the model to all wind tunnel and Navier Stokes CFD data currently available.[11]

5. References

1. Murphy CH. Generalized subharmonic response of a missile with slight configurational asymmetries. Army Ballistics Research Laboratory (US); 1972 June. Report No.: 1591.

2. Morote J, Morote P. Catastrophic yaw of triform and cruciform-tailed missiles. J Spacecraft Rockets. 2018 Jan-Feb;55(1):245–248.

3. Morote J. Control of roll lock-in and catastrophic yaw for cruciform finned missiles. AIAA Atmospheric Flight Mechanics Conference; 2009 Aug 10–13; Chicago, IL. AIAA 2009-5715. doi: 10.2514/6.2009-5717.

4. Pepitone TR, Jacobson ID. Resonant behavior of a symmetric missile having roll orientation dependent aerodynamics. J Guidance Control. 1978;1(5):335–339.

5. Vasile JD, Bryson JT, Fresconi FE. Aerodynamic design optimization of long range projectiles using missile DATCOM. DEVCOM Army Research Laboratory (US); 2020 Apr. Report No.: ARL-TR-8936.

6. Bryson JT, Vasile JD, Gruenwald, BC, Sahu, J, and Fresconi, F, Modeling and flight dynamics of a projectile with nonlinear, roll-dependent aerodynamics. AIAA SciTech Forum; 2021 Jan 11–15 & 19–21. Virtual Event. doi: 10.2514/6.2021-0823.

7. Vasile J, Bryson J, Sahu J, Paul J, Gruenwald B. Aerodynamic dataset generation of a long range projectile. DEVCOM Army Research Laboratory (US); 2020 Aug. Report No.: ARL-TR-9019.

8. Vasile JD, Sahu J. Roll orientation–dependent aerodynamics of a long-range projectile. DEVCOM Army Research Laboratory (US); 2020 Aug. Report No.: ARL-TR-9017.

9. Pokela R, Kumar R, Vasile J. Experimental and computational aerodynamic characterization of a generic high-speed projectile configuration. Submitted to the 2021 AIAA Aviation Forum; under review.

10. Aftosmis MJ, Berger MJ, Adomavicius G. A parallel multilevel method for adaptively refined Cartesian grids with embedded boundaries. Proceedings of the 38th AIAA Aerospace Sciences Meeting and Exhibit; 2000; Reno, NV. AIAA Paper No.: 2000-0808.

11. Burchett BT, Vasile JD, Bryson JT. Combining sparse and dense databases to form a robust aerodynamic model for a long-range, high-speed projectile. Submitted to the 2022 AIAA SciTech Forum; under review.

Appendix. Converting between Cartesian and Polar Fourier

Fourier coefficients for the wind tunnel data had to be determined in Cartesian form, since the data contained less than a full "period". In order to compare these coefficients to those found from the Cart3D estimates, we need to map between the polar and Cartesian forms. The wind tunnel Fourier series is found in the Cartesian form

$$\hat{y} = \frac{a_0}{2} + \sum_{n=1}^{\infty} (a_n \cos 2\pi n \cdot \phi/T + b_n \sin 2\pi n \cdot \phi/T) \tag{A-1}$$

where the C3D estimates were smoothed with a Polar form:

$$\hat{y} = X_0 + 2 \sum_{n} |X_n| \cos(2\pi n \cdot \phi/T + \angle X_n) \tag{A-2}$$

Thus, the biases are easily equated. Since cos and sin are orthogonal, the Pythagorean theorem may be used to write

$$|X_n| = \sqrt{a_n^2 + b_n^2} \tag{A-3}$$

and likewise

$$\angle X_n = -\tan^{-1} \frac{b_n}{a_n} \tag{A-4}$$

Since the wind tunnel estimates are for the entire vehicle in various configurations, superposition will need to be applied to the C3D Fourier terms in order to form a valid comparison. So instead of mapping from Cartesian to polar, we will need to do the inverse. We begin by squaring Eq. 28 to get

$$|X_n|^2 = a_n^2 + b_n^2 \tag{A-5}$$

Manipulating Eq. 29, we can get

$$a_n \cdot \tan(-\angle X_n) = b_n \tag{A-6}$$

and

$$a_n^2 \cdot \tan^2(-\angle X_n) - b_n^2 = 0 \tag{A-7}$$

Equations 30 and 32 can be solved simultaneously for the squares of the Cartesian amplitudes, and Eq. 31 will give the *relative* signs between them; however, that leaves two possible solutions. Thus, we use the quadrant of $\angle X_n$ to disambiguate the signs by

$$a_n = \text{sign}(\cos(-\angle X_n)) \cdot \sqrt{a_n^2} \tag{A-8}$$

and

$$b_n = \text{sign}(\sin(-\angle X_n)) \cdot \sqrt{b_n^2} \tag{A-9}$$

List of Symbols, Abbreviations, and Acronyms

3-D	three-dimensional
AoA	angle of attack
CFD	computational fluid dynamics
CG	center of gravity
LTV-1	Laboratory Technology Vehicle
MAS	moving aerodynamic surface
NASA	National Aeronautics and Space Administration
RAS	rigid aerodynamic surface
$\{\phi, \theta, \psi\}$	projectile roll, pitch, and yaw in local ground frame (rad)
$\lvert X_n \rvert \angle X_n$	magnitude/phase of polar Fourier harmonic *n*
T	period of harmonic function (rad)
$\mathbf{I}$	identity matrix
a_n, b_n	Cartesian Fourier amplitudes
i	$= \sqrt{-1}$
M	Mach number
$\mathbf{\Phi}$	Matrix of harmonic basis functions
ϑ	placeholder, $\vartheta \in \{A, S, N, l, m, n\}$
$\mathbf{R}$	rotation matrix
α	angle of attack (deg)
δ	flap deflection (deg)
$f(.)$	function to be approximated
D	projectile diameter (m)
C_A	axial force coefficient
C_S	side force coefficient
C_N	normal force coefficient
C_l	roll moment coefficient

C_m	pitch moment coefficient
C_n	yaw moment coefficient

Subscript

$90°$	$90°$ rotation
n	harmonic number

Superscript

T	matrix transpose
L	placeholder, $L \in \{R, M_1, M_2, M_3, M_4\}$
R	rigid aerodynamic surface
M_j	moving aerodynamic surface j
B	body frame
WT	wind tunnel frame
N	normal force component
S	side force component

1 (PDF) DEFENSE TECHNICAL INFORMATION CTR DTIC OCA

1 (PDF) DEVCOM ARL FCDD RLD DCI TECH LIB

1 (PDF) DEVCOM AC RDAR-MEM-A M DUCA

3 (PDF) DEVCOM AVMC FCDD AMS MMA J DOYLE C ROSEMA M MCDANIEL

1 (PDF) JHU/APL A NEDUNGADI

1 (PDF) SNL C SMITH

1 (PDF) FSU R KUMAR

29 (PDF) DEVCOM ARL FCDD RLW J ZABINSKI FCDD RLW A F FRESCONI FCDD RLW D L D FAIRFAX FCDD RLW ME S SILTON FCDD RLW TE R SUMMERS FCDD RLW W W OBERLE P PEREGINO T SHEPPARD FCDD RLW WA N TRIVEDI E BYRD FCDD RLW WB J SADLER FCDD RLW WC A WILLIAMS M NUSCA A MCBAIN M MINNICINO FCDD RLW WD V BHAGWANDIN B GRUENWALD I CELMINS J SAHU B BURCHETT J PAUL J VASILE J BRYSON L STROHM J DESPIRITO FCDD RLW WE M ILG B TOPPER D EVERSON T BROWN